



Ruddlesden-Popper compounds in the double-perovskite family $\text{Sr}_2\text{FeTaO}_6(\text{SrO})_n$ ($n = 0, 1$ and 2) and their photocatalytic properties

Hongmei Chen, Xiaoxiang Xu*

Shanghai Key Lab of Chemical Assessment and Sustainability, School of Chemical Science and Engineering, Tongji University, 1239 Siping Road, Shanghai 200092, China

ARTICLE INFO

Article history:

Received 24 October 2016

Received in revised form

25 December 2016

Accepted 4 January 2017

Available online 5 January 2017

Keywords:

Double perovskite

Ruddlesden-Popper compound

Photocatalyst

Hydrogen production

ABSTRACT

Defects control and structural modifications are useful tools in tailoring the photocatalytic activity of a semiconductor. In this work, we demonstrate how defects removal and structural lamination control the photocatalytic performance of double perovskite $\text{Sr}_2\text{FeTaO}_6$ and its layered derivatives – Ruddlesden-Popper (RP) compounds $\text{Sr}_3\text{FeTaO}_7$ and $\text{Sr}_4\text{FeTaO}_8$. Our results show that high oxidation state Fe defects are involved during the high temperature synthesis of these compounds. A simple thermal treatment in the presence of ethylene glycol effectively removes these defects and turns their color from dark green to bright yellow while still maintaining their crystal structures and microstructures. Further experiments on photocatalysis reveal the critical role of thermal treatment in terms of boosting photocatalytic hydrogen production almost 3-fold for all samples under full range irradiation (≥ 250 nm). The highest activity under full range irradiation belongs to $\text{Sr}_2\text{FeTaO}_6$, which gives an average hydrogen production rate $\sim 107 \mu\text{mol}/\text{h}$, corresponding to apparent quantum efficiency (AQE) $\sim 1.36\%$. More importantly, visible light photocatalytic hydrogen production was also realized after thermal treatment with the highest AQE $\sim 0.54\%$ for $\text{Sr}_4\text{FeTaO}_8$. Theoretical calculations indicate the anisotropic feature of RP compounds for charge migrations and highlight the benefits of structural lamination by reducing inter-layer charge recombination. Our work here signifies the importance of defect control and offers some clues for the design of efficient photocatalysts by means of structural modifications.

© 2017 Elsevier B.V. All rights reserved.

1. Introduction

Searching renewable and clean energy resources has been an urgent task for us in the 21st century, not only because of our ever-growing energy demand yet a severe shortage of fossil fuels but also due to the increasing awareness of environmental issues associated with fossil fuel usage [1–3]. In these contexts, photocatalytic water splitting into hydrogen and oxygen, driven by solar energy, has been considered as a promising scenario for establishing renewable energy infrastructure as hydrogen is a clean energy vector and solar insolation is inexhaustible in nature and widely distributed all over the world [4–11]. After decades of effort devoted to searching and developing efficient photocatalytic materials (mainly semiconductors), very few compounds demonstrate solar-to-hydrogen efficiency (STH) high enough to warrant practical deployment [12–14]. This is mainly because most stable semiconductors (generally oxides) own a band gap too large

to enable appreciable absorption of solar energy whose spectrum spreads mostly in visible and infrared region [15,16]. Therefore, band gap control for photocatalytic semiconductors plays a pivotal role for achieving a high STH [15,17–19]. For instance, a band gap reduction from 3.2 eV to 2.1 eV will increase the theoretical STH from less than 1% to nearly 16% [15]. Recent studies have witnessed a number of successes in band gap reduction and visible light photocatalysis by means of doping techniques, i.e. introducing foreign atoms (usually transition metals with partially filled *d* orbitals) into wide band gap semiconductors [20]. Those transition metals normally formed a new valence band inside the original band gap thereby significantly reduce the threshold for light absorption and photocatalysis due to the involvement of transition metal *d* electrons [21–25]. On the other hand, oxides with perovskite-type structure (ABO_3) often show promising catalytic activity [26–28]. In particular, perovskite oxides containing Ta are efficient photocatalysts for water splitting under band gap excitations [29–33]. For instance, La modified NaTaO_3 exhibit apparent quantum efficient as high as 56% at 270 nm for water splitting [34]. Perovskite compounds are well-known for their diversification in composition and crystal structures [35]. By altering internal constituent elements

* Corresponding author.

E-mail addresses: xxxu@tongji.edu.cn, xiaoxiangx@gmail.com (X. Xu).



such as cation off-stoichiometry (e.g. A-site deficiency) [4] and diverse B-site cations (e.g. complex perovskites) [9,28,36] or modifying atom arrangement such as atomic ordering/disordering and structural lamination (e.g. layered perovskites) [9,21,31], various physicochemical properties can be tuned in order to meet different applications. Previous research indicates that complex perovskites containing Ta are promising photocatalysts for water splitting and layered perovskites are capable of rectifying charge transportation [21,37,38]. In this work, we performed an investigation on the double-perovskite compound $\text{Sr}_2\text{FeTaO}_6$ and its layered derivatives – Ruddlesden-Popper (RP) compounds $\text{Sr}_3\text{FeTaO}_7$ and $\text{Sr}_4\text{FeTaO}_8$ for photocatalytic hydrogen production reactions. The involvement of Fe in the structure with partially filled d orbitals may suggest visible light photocatalytic activity and structural modification from pristine perovskite to layered ones offers an ideal case to study the correlations between structural amendment and photocatalytic activity.

2. Experimental

2.1. Material synthesis

$\text{Sr}_2\text{FeTaO}_6(\text{SrO})_n$ ($n=0\text{--}2$) were synthesized by a polymeric citrate precursor method according to the previous literature [22]: appropriate amounts of tantalum chloride (Alfa Aesar, 99.99%), strontium nitrate (SCR, $\geq 99.5\%$) and iron (III) nitrate (SCR, $\geq 98.5\%$) was dissolved into 20 mL ethanol (SCR, $\geq 95\%$). The above solution was further added with 10 mL ethylene glycol and 5 g citric acid with magnetic stirring to completely dissolve the reagents. Proper thermal treatment (200°C for 2 h) was applied to the solution to promote polymerization. The solution was dried and was turned into brown resin after the treatment. The resin was calcined at 500°C in air for 12 h to remove organic species and was ground into fine powders. The powders were then uniaxially pressed into pellets under a pressure of 5 t and calcined at 1000°C for 12 h. Higher temperatures 1200°C and 1400°C was needed to produce single phase of Ruddlesden-Popper (RP) compounds $\text{Sr}_3\text{FeTaO}_7$ ($n=1$) and $\text{Sr}_4\text{FeTaO}_8$ ($n=2$), respectively. The calcined pellets were ground into powders and collected for further treatment or analysis.

Reduction of as-prepared samples was carried out by dispersing sample powders into ethylene glycol at 200°C for 1 h. The reduced sample powders were then washed with deionized water for 3 times and dried at 80°C for 10 h. These powders were labelled as r- $\text{Sr}_2\text{FeTaO}_6$, r- $\text{Sr}_3\text{FeTaO}_7$ and r- $\text{Sr}_4\text{FeTaO}_8$ to be discriminated from their pristine powders.

2.2. Methods for analysis

Crystal structure and phase purity were analyzed by using X-ray powder diffraction (XRD) techniques on Haoyuan DX-2700B diffractometer. Incident X-ray radiation was $\text{Cu K}_{\alpha 1}$ ($\lambda = 1.5406\text{\AA}$) and $\text{Cu K}_{\alpha 2}$ ($\lambda = 1.5444\text{\AA}$) respectively. The step size for data collection was 0.02° with a collection time of 1 s. The General Structure Analysis System (GSAS) software package was adopted to perform Rietveld refinement. Microstructures of all samples were examined using a field emission scanning electron microscope (Hitachi S4800) and a transmission electron microscope (JEOL JEM-2100). Diffuse reflectance spectra were collected using a UV-vis spectrophotometer (JASCO-750) and analyzed using JASCO software suite with barium sulfate as a reference non-absorbing material. Surface areas of all samples were measured by using a micromeritics instrument (Quanta chrome Nova 2200e) and were calculated by using the Brunauer–Emmett–Teller (BET) model. Surface chemical compositions and constituent element binding energy of all samples were analyzed using X-ray photoelectron microscopy (AXIS

Ultra DLD with a monochromatic Al K_{α} X-ray source). All binding energies were referenced to the C 1s peak at 284.7 eV arising from adventitious carbon [39].

2.3. Photocatalytic hydrogen production

A top-irradiation-type reactor with a gas closed circulation and evacuation system (Perfect Light, Lab solar – IIIAG) were used to evaluate the Photocatalytic hydrogen production of as-prepared samples. Water jacket was used to stabilize the reactor temperature around 20°C and gas component within the reactor was analyzed using an on-line gas chromatograph (TECHCOMP, GC7900) with a TCD detector (5 Å molecular sieve columns and Ar carrier). In a typical measurement, 100 mg sample powders were dispersed into 100 mL sodium sulfite solution (0.05 M). 1 wt% platinum was loaded onto the sample powders through a thermal deposition method: appropriated amounts of H_2PtCl_6 aqueous solution was impregnated into sample powders to form slurries. The slurries were heated at 90°C until dry and calcined at 180°C to fully convert H_2PtCl_6 into Pt. A 500 W high-pressure mercury lamp (NBET, Merc-500) was used as a light source and visible light irradiation was obtained by filtering the output of the lamp with a UV cutoff filter ($\lambda \geq 400\text{ nm}$). The photon flux of the lamp was calibrated using a quantum meter (Apogee MP-300). the recorded photon flux is $\sim 1543.9\text{ }\mu\text{mol/m}^2/\text{s}$ for full range irradiation and $\sim 796.5\text{ }\mu\text{mol/m}^2/\text{s}$ for visible light irradiation ($\lambda \geq 400\text{ nm}$). The apparent quantum efficiency (AQE) is then calculated using the following equation:

$$\text{Apparent quantum efficiency} = \frac{2 \times \text{mol of hydrogen}}{\text{production per hour} / \text{moles of photon flux per hour}} \times 100\%$$

2.4. Theoretical calculations

Theoretical calculations were carried out using density functional theory (DFT) implemented in the Vienna Ab initio Simulation Package (VASP) [40]. The Perdew, Burke and Ernzerhof (PBE) exchange-correlation functional within the generalized gradient approximation (GGA) [41] and the projector augmented-wave pseudopotential were used [42]. A unit cell ($a = 5.63\text{\AA}$, $b = 5.62\text{\AA}$, $c = 7.94\text{\AA}$, $\alpha = \beta = \gamma = 90^\circ$) with orthorhombic symmetry and a unit cell ($a = b = 3.95\text{\AA}$, $c = 12.68\text{\AA}$, $\alpha = \beta = \gamma = 90^\circ$) with tetragonal symmetry were built for $\text{Sr}_2\text{FeTaO}_6$ and $\text{Sr}_4\text{FeTaO}_8$ simulations. All geometry structures were fully relaxed until the forces on each atom are less than 0.01 eV/\AA . Static calculations were done with $9 \times 9 \times 6$ and $13 \times 13 \times 4$ Monkhorst-Pack k -point grid for $\text{Sr}_2\text{FeTaO}_6$ and $\text{Sr}_4\text{FeTaO}_8$ respectively [43].

3. Results and discussions

3.1. Phase purity and crystal structure

X-ray powder diffraction patterns of as-prepared samples and their refined data are illustrated in Figs. 1 and 2. All patterns can be indexed using a proper symmetry, indicating the formation of a single phase. Patterns for double perovskite compound $\text{Sr}_2\text{FeTaO}_6$ was indexed using an orthorhombic symmetry due to the presence of tiny peaks around 25° and 35° , consistent with previous report (JCPDS No. 01-088-0135). While for RP compounds, a tetragonal symmetry was adopted to fully index all diffraction peaks, in agreement with previous observations (JCPDS No. 00-032-1238, 00-052-1716). Super-lattice peaks arising from cation ordering at the B sites (i.e. Fe and Ta) were not observable for these samples and reasonable goodness-of-fit parameters for the

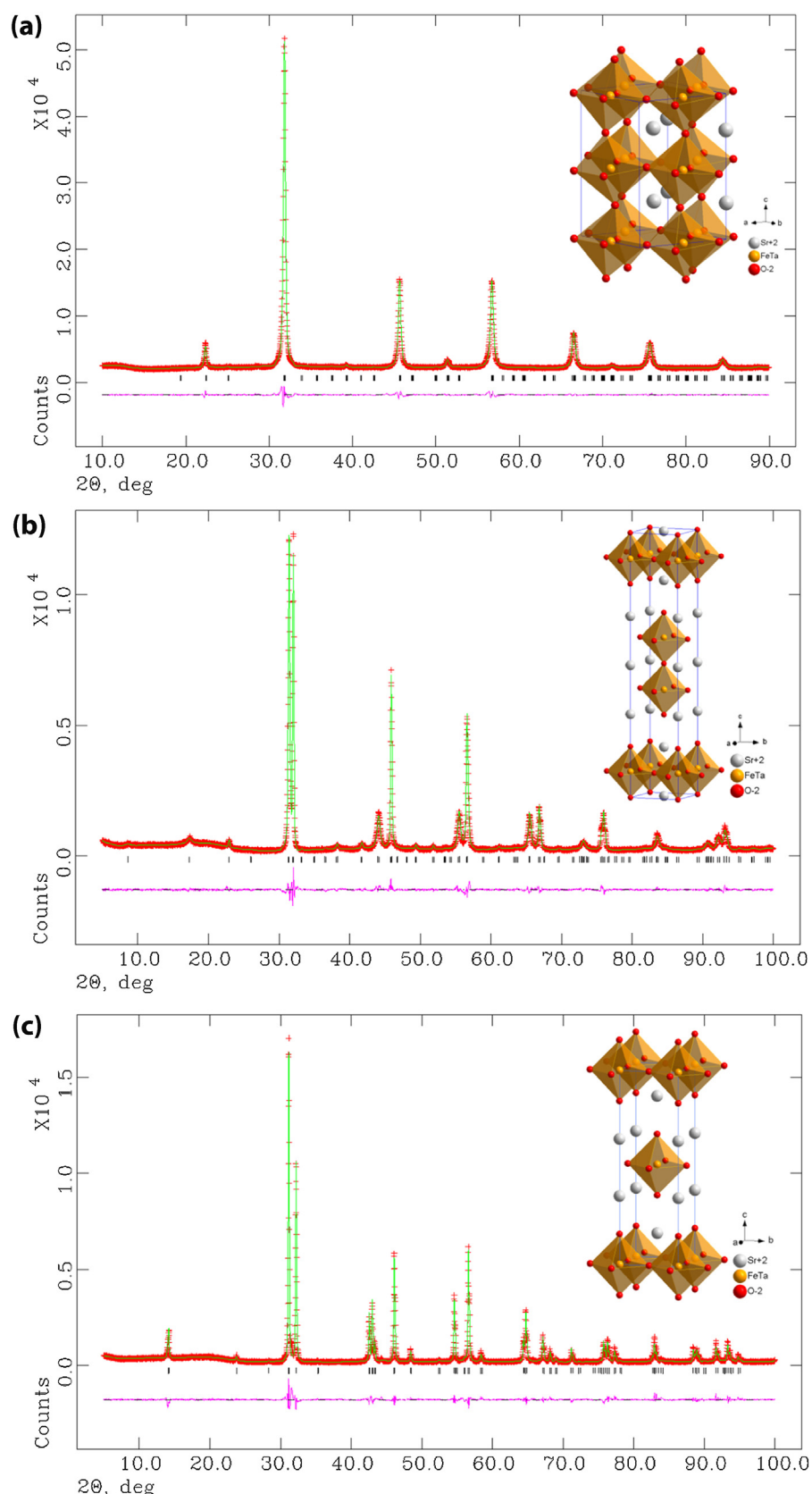
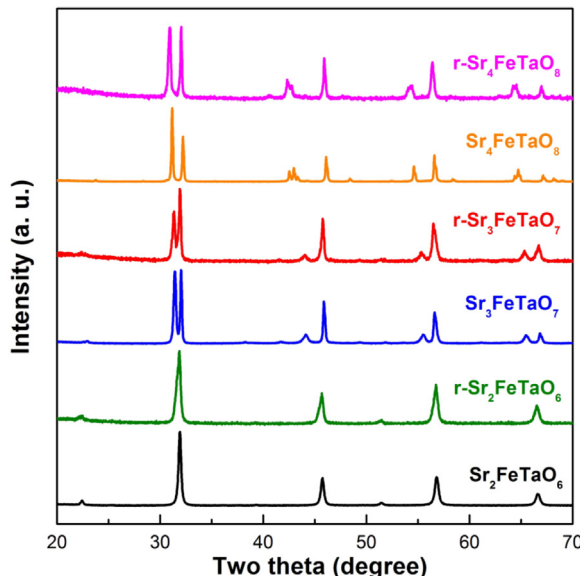


Fig. 1. Observed and calculated X-ray powder diffraction patterns of (a) $\text{Sr}_2\text{FeTaO}_6$, the refinement converged with good R-factors ($R_p = 2.06\%$, $R_{wp} = 2.91\%$, $\chi^2 = 2.386$), (b) $\text{Sr}_3\text{FeTaO}_7$, the refinement converged with good R-factors ($R_p = 5.26\%$, $R_{wp} = 7.03\%$, $\chi^2 = 2.394$) and (c) $\text{Sr}_4\text{FeTaO}_8$, the refinement converged with good R-factors ($R_p = 6.91\%$, $R_{wp} = 9.75\%$, $\chi^2 = 3.967$). The refined crystal structures are shown in the inset images.

Table 1

Unit cell parameters and band gap values of as-prepared samples (Standard deviation in parentheses).

	Space group	a/Å	b/Å	c/Å	V/Å ³	Band gap/eV
Sr ₂ FeTaO ₆	P bnm	5.6325(7)	5.6228(6)	7.9487(8)	251.74(2)	–
Sr ₃ FeTaO ₇	I 4/mmm	3.9632(1)	–	20.5798(7)	323.26(2)	–
Sr ₄ FeTaO ₈	I 4/mmm	3.9531(1)	–	12.6813(3)	198.17(1)	–
r-Sr ₂ FeTaO ₆	P bnm	5.640(2)	5.630(2)	7.951(3)	252.46(8)	2.01
r-Sr ₃ FeTaO ₇	I 4/mmm	3.9668(2)	–	20.598(3)	324.12(4)	2.21
r-Sr ₄ FeTaO ₈	I 4/mmm	3.9493(4)	–	12.727(2)	198.50(6)	2.27

**Fig. 2.** X-ray powder diffraction patterns of as-prepared samples before and after reduction.

refinement was only achieved by setting a constrain that Fe and Ta occupy the same crystallographic position, confirming a random distribution of cations at the B sites. According to the Rietveld refinement, double perovskite compound Sr₂FeTaO₆ largely maintains the ideal perovskite structure by corner-sharing the Fe(Ta)O₆ octahedrons to form a three-dimensional network (Fig. 1). Its symmetry degradation from cubic to orthorhombic stems from the tilting of Fe(Ta)O₆ octahedrons perpendicular to the c direction (Glazer notation $a^-b^-c^0$). Whereas these tilts were fully relaxed in the RP compounds Sr₃FeTaO₇ and Sr₄FeTaO₈, probably due to the removal of octahedron connectivity along c direction and insertion of extra SrO layers that releases somewhat tensions inside the structures. The structural difference between Sr₃FeTaO₇ (n = 1) and Sr₄FeTaO₈ (n = 2) arises from a different manner of SrO layer insertion along c direction, either by every two layers of Fe(Ta)O₆ octahedrons for Sr₃FeTaO₇ (n = 1) or by every single layer in case of Sr₄FeTaO₈ (n = 2). The freshly prepared samples after high temperature calcination are all dark green, implying high oxidation state of Fe or oxygen non-stoichiometry. A thermal treatment in ethylene glycol at 200 °C for 1 h (reduction) effectively turns their color into yellow by reducing those defects, as will see in the following session. XRD analysis suggests that their diffraction patterns are all retained after reduction (Fig. 2). Nevertheless, peak shift and variation in peak intensity was observed, especially for RP compounds. This can be explained by the reduction of high oxidation state Fe species that greatly modifies the electron density distribution inside the structure as X-ray diffraction techniques are electron sensitive [44]. Further refinement on their unit cell parameters confirms a slight expansion of their unit cells and is attributed to a larger ionic radius of Fe cations after reduction (Table 1).

3.2. UV-vis spectroscopy

The strong dark green color of high temperature calcined samples suggests the presence of high oxidation state Fe species inside the structure [45]. This is confirmed from their UV-vis absorption spectra that strong light absorption covers entire spectroscopic range (Fig. 3). However, after a thermal treatment in ethylene glycol, all samples turn into yellow color and UV-vis absorption spectra reveal a clear absorption edge around 600 nm, indicative of semiconductivity. Such a dramatic color change before and after reduction treatment mainly comes from the depression of light absorption above 500 nm which has been frequently attributed to defects with unpaired electrons (e.g. Fe⁴⁺ etc.) [45]. It is known that hot ethylene glycol serves as a powerful reducing agent; therefore, a thermal treatment in ethylene glycol is effective to remove high oxidation state Fe species. The band gap values of all three samples after reduction were then calculated using Kubelka-Munk transformation by extrapolating the tangent of absorption edges. Double perovskite compound r-Sr₂FeTaO₆ owns the smallest band gap ~2.0 eV and there is a slight enlargement in band gap values if the level of structural lamination increases, i.e. from 2.2 eV to 2.3 eV for r-Sr₃FeTaO₇ and r-Sr₄FeTaO₈, respectively (Fig. 3).

3.3. Microstructures

The microstructure of as-prepared sample powders were then examined using a field-emission scanning electron microscopy (FESEM). Fig. 4 displays the SEM images of samples after reduction treatment. r-Sr₂FeTaO₆ typically exhibits featureless particles with particle size of several microns, a common observation after high temperature calcination. Contrarily, RP compounds demonstrate laminal textures that are strongly correlated with their crystal structures (Fig. 4c–f). r-Sr₃FeTaO₇ exhibit plate-like particles that randomly stack with each other. These plate-like particles are likely peeled off from bulky particles and contribute to a high surface area ~21.432 m² g⁻¹ observed. Nevertheless, r-Sr₄FeTaO₈ displays large bulky particles, but its layered crystal structure can be easily inferred from the laminal terrace at the particle surface (indicated by the yellow arrows in Figure e and f). The microstructures of all samples before and after reduction treatment were compared in Fig. S1. No significant difference in terms of particle size and surface textures were observable thereby microstructures of all samples were maintained after reduction. The microstructure of r-Sr₄FeTaO₈ was further analyzed using transmission electron microscopy (TEM). A typical high-resolution TEM image (HRTEM) showing (002) lattice fringes was displayed in Fig. 5. Its laminated crystal structure can be easily identified by the periodical insertion of dark and white fringes in the image (marked by the yellow arrow in Fig. 5). A representative crystal structure of Sr₄FeTaO₈ (projected from [100] direction) was illustrated on the right hand side of Fig. 5, which closely matched the laminated microstructures in the TEM image. Microstructures of all samples before and after reduction were examined by HRTEM where no discernable structure changes can be identified, confirming the maintenance of crystal structure during reduction (Fig. S2).

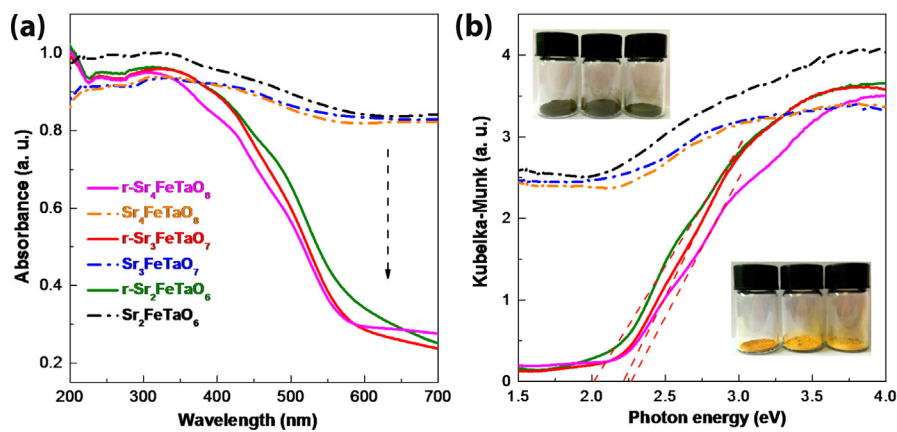


Fig. 3. (a) UV-vis light absorption spectra (converted from diffuse reflectance spectra) of samples before and after reduction and (b) Kubelka-Munk transformation of diffuse reflectance data, digital photographs of samples before and after reduction are inserted (left to right are Sr₂FeTaO₆, Sr₃FeTaO₇ and Sr₄FeTaO₈).

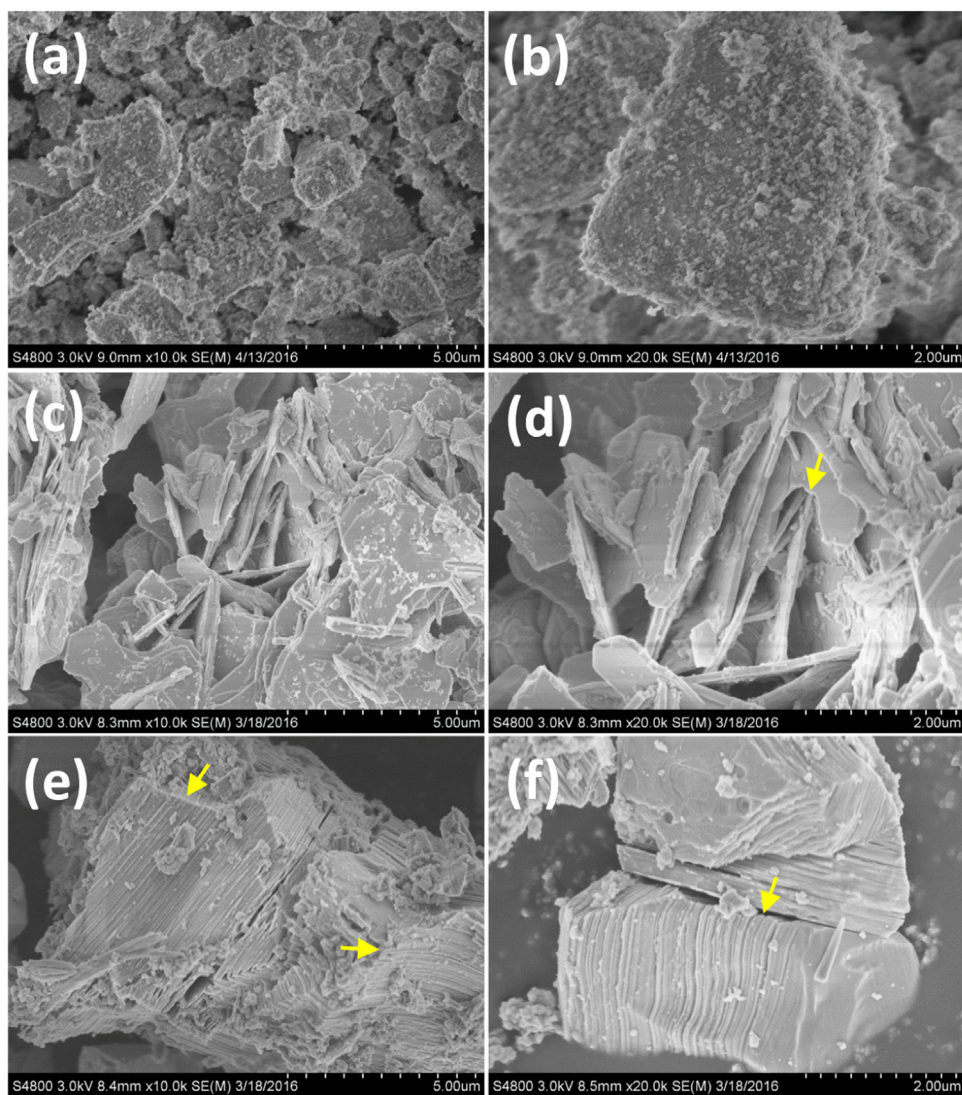


Fig. 4. Field emission scanning electron microscopy images of r-Sr₂FeTaO₆ (a, b), r-Sr₃FeTaO₇ (c, d) and r-Sr₄FeTaO₈ (e, f), laminated microstructures are indicated by the yellow arrow. (For interpretation of the references to colour in this figure legend, the reader is referred to the web version of this article.)

3.4. X-ray photoelectron spectroscopy (XPS)

The surface nature of all samples before and after reduction was then analyzed using X-ray photoelectron spectroscopy (XPS). Bind-

ing energy of core-level electrons of constituent elements such as O and Fe is illustrated in Fig. 6. All data were referenced to C 1s peak at 284.7 eV, arising from adventitious carbon. Overlapping peaks were unfolded by fitting with different Gaussian functions. O 1s sig-

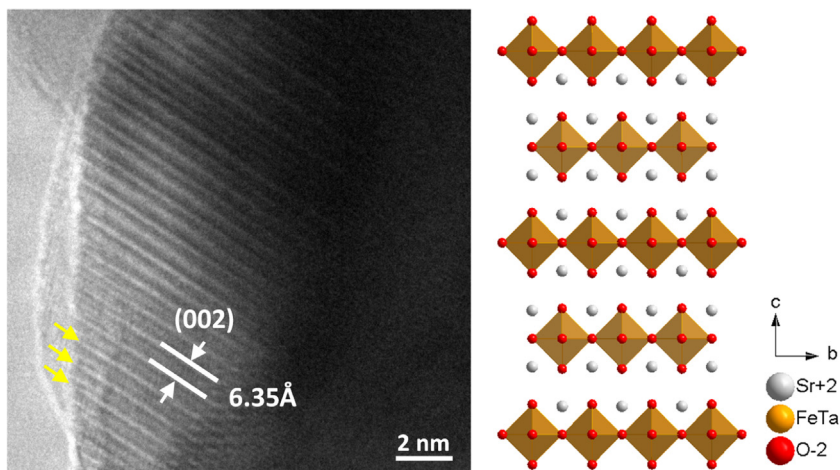


Fig. 5. High-resolution transmission electron microscopy image of $\text{Sr}_4\text{FeTaO}_8$ after reduction, (002) lattice fringe is marked and a representative crystal structure is illustrated on the right for visual inspection.

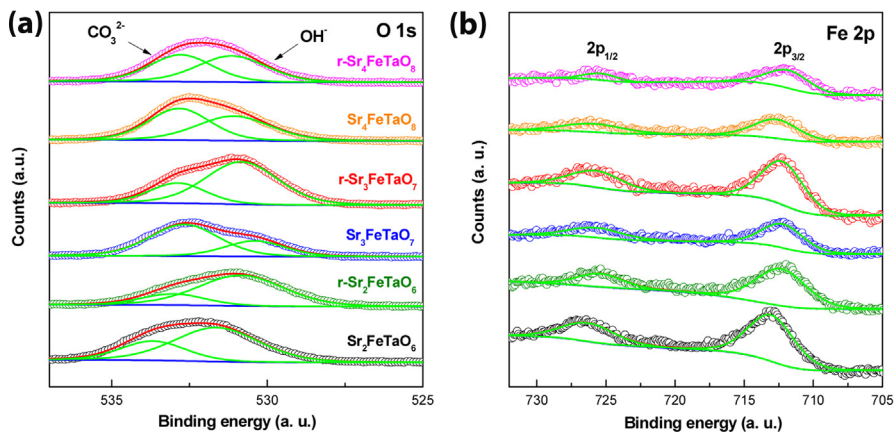


Fig. 6. XPS spectra of samples before and after reduction: (a) O 1s peaks and (b) Fe 2p peaks.

nal generally contains two overlapping peaks at 531 eV and 533 eV, assignable to surface OH^- and CO_3^{2-} groups. Reduction in ethylene glycol seems to favor the growth of surface OH^- groups as can be seen from the increase of peak at 531 eV after reduction. The lattice oxygen signal, normally appearing at 529 eV, is indiscernible for all samples, suggesting a fully covered surface. Likewise, the Fe 2p signal contains two separated peaks at around 712 eV and 726 eV, corresponding to Fe 2p_{3/2} and Fe 2p_{1/2} states due to spin-orbital splitting. However, a lightly shift of these peaks to a lower binding energy can be noticed for samples after reduction, which may correlate to a change of oxidation state of Fe. Nevertheless, signals for Fe with high oxidation state (e.g. Fe^{4+}) is not observed here and is likely due to the detection limit of XPS that only reaches a depth of 1–3 nm at the surface.

3.5. Photocatalytic hydrogen production

The photocatalytic properties of double perovskite $\text{Sr}_2\text{FeTaO}_6$ and its RP derivatives were evaluated by monitoring their hydrogen production in the presence of sacrificial agent under light irradiation. Here, Pt (1 wt%) and sodium sulfite (0.05 M) aqueous solution were used as a cocatalyst and a hole scavenger respectively to promote photo-reduction reactions. Control experiments with either samples or light irradiation missing did not give a detectable hydrogen signal therefore precluding any spontaneous hydrogen production reactions. Immediate hydrogen evolution was detected when light was illuminated upon these samples, indicative of a

real photocatalytic process. Temporal hydrogen production for all samples recorded under full range irradiation ($\lambda \geq 250 \text{ nm}$) was showed in Fig. 7a. It can be seen from Fig. 7a that samples before reduction exhibit only mild hydrogen production. Less than $100 \mu\text{mol}$ hydrogen was produced within 3 h irradiation period. On the contrary, hydrogen production was significantly boosted for samples after reduction with at least three-fold enhancement in all cases. For instance, more than $300 \mu\text{mol}$ hydrogen was produced for r- $\text{Sr}_2\text{FeTaO}_6$, which exceeds the amount of catalyst used ($\sim 196 \mu\text{mol}$), confirming an efficient photocatalytic reaction. Presumably, such an improvement over catalytic activity arises from the elimination of high oxidation state Fe species which may trap or consume photo-generated electrons [21,46–48]. More importantly, hydrogen production under visible light irradiation was also achieved for these reduced samples, highlighting the benefit of reduction treatment. The average photocatalytic hydrogen production rate for reduced samples under both full range and visible light irradiation ($\lambda \geq 400 \text{ nm}$, $\lambda \geq 420 \text{ nm}$) were plotted in Fig. 7b and Fig. S3. All reduced samples display comparable activity under full range irradiation and the highest activity belongs to r- $\text{Sr}_2\text{FeTaO}_6$, which gives an average hydrogen production rate $\sim 107 \mu\text{mol}/\text{h}$, corresponding to apparent quantum efficiency (AQE) $\sim 1.36\%$. Surface area does not seem to play a dominant role here as a large surface area does not guarantee a high activity (Table S1). However, a strong correlation between layered structure and visible light photocatalytic activity was recognized as RP compounds all exhibit a better performance than double perovskite compound

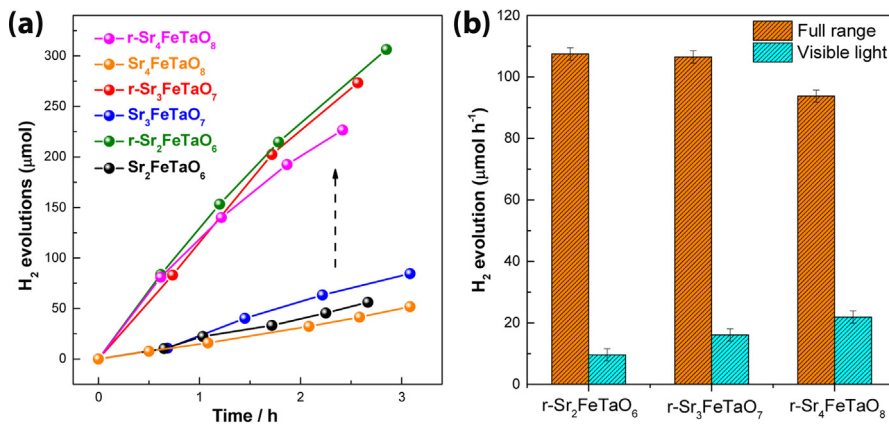


Fig. 7. (a) photocatalytic hydrogen production of samples before and after reduction under full range irradiation ($\lambda \geq 250$ nm) in sodium sulfite aqueous solution (0.05 M) and (b) average photocatalytic hydrogen production rate under full range irradiation ($\lambda \geq 250$ nm) and visible light irradiation ($\lambda \geq 400$ nm) for reduced samples r-Sr₂FeTaO₆, r-Sr₃FeTaO₇ and r-Sr₄FeTaO₈, respectively.

(Fig. 7b and Fig. S3). Sample with the highest level of lamination within the structure (i.e. r-Sr₄FeTaO₈) demonstrates the highest hydrogen production rate $\sim 22 \mu\text{mol}/\text{h}$ under visible light irradiation ($\lambda \geq 400$ nm), corresponding to apparent quantum efficiency (AQE) $\sim 0.54\%$. Considering the low concentration of transition metals (i.e. Fe and Ta) inside RP compounds than double perovskite Sr₂FeTaO₆, such an enhancement in visible light photocatalytic activity is significant. An intuitive question therefore arises as how does structural lamination promote visible light photocatalytic activity rather than those under full range irradiation.

3.6. Theoretical calculations

To solve the aforementioned question, we performed theoretical calculations on the electronic structure of double perovskite Sr₂FeTaO₆ and RP compound Sr₄FeTaO₈. The calculated results are displayed in Fig. 8 which shows the band structure and density of states (DOS) near Fermi level. For double perovskite Sr₂FeTaO₆, theoretical calculations suggest an indirect band gap of ~ 0.17 eV, confirming its semiconductivity. Although this calculated band gap value is considerably smaller than experimental one (>2.0 eV), likely due to shortcomings of the generalized gradient approximation (GGA) method for underestimating band gaps, the calculations have qualitative significance. On the contrary, RP compound Sr₄FeTaO₈ does not seem to have a clear band gap according to calculated results as Fermi level lies inside a band which is mainly composed of Fe 3d orbitals. Nevertheless, considering the very localized nature of Fe 3d electrons, Sr₄FeTaO₈ is essentially a semiconductor according to the Hubbard model [49]. More importantly, band structure of RP compound Sr₄FeTaO₈ reveals a strong anisotropic feature for electron migration, strikingly different from double perovskite Sr₂FeTaO₆. For instance, from Γ to Σ governs the electron behavior in [100] crystallographic direction and bands close to Fermi level all exhibit a large energy dispersion (Fig. 8b). Contrarily, all bands are nearly pinned at constant energy levels from X to P which controls electron behavior along [001] direction. It is known that the effective mass (m^*) of charge carriers (electrons or holes) is proportional to the second derivatives of E versus k curve (i.e. wide band gives small m^*) [50,51]:

$$m^* = \hbar^2 \left(\frac{d^2 E}{dk^2} \right)^{-1}$$

Therefore, electrons/holes are allowed to migrate along [100] direction but are forbidden to transport along [001] direction. Close examination on other crystallographic directions suggest that electron migration is allowed for all directions that are perpendicular

to c axis, i.e. intra-layer transport is allowed rather than inter-layer. Considering the fact that bands close to Fermi level are mainly composed of Fe 3d, Ta 5d and O 2p orbitals, electrons/holes thus are only allowed to move within laminated layers containing Fe(Ta)O₆ octahedrons. Similar anisotropic feature has been realized in other layered compounds such as Sr₂TiO₄ and Zn_nIn₂O_{3+n} ($n = 4, 5$ and 7) [21,52]. Such a confinement for charge transport along laminated layers is highly beneficial for photocatalytic reactions as inter-layer charge recombination is prohibited and charge carriers have a higher chance to approach surface reaction sites [21].

The band edge positions for samples after reduction were then quantitatively determined by electrochemical method. Fig. 9a displayed a Mott-Schottky plot for the prepared photoelectrodes. All samples show a positive slope in the linear region, indicative of *n*-type semiconductivity. The flat band potential, determined from the extrapolation of the linear curve to the axis, arranges in the order of -0.16 V, -0.20 V and -0.27 V for r-Sr₂FeTaO₆, r-Sr₃FeTaO₇ and r-Sr₄FeTaO₈. Thereby, the band edge positions (i.e. conduction band (CB) and valence band (VB) edges) can be easily calculated from UV-vis spectra data (Table 1), assuming that flat band potential lies closely to CB edge. As shown in Fig. 9b, r-Sr₄FeTaO₈ owns the most negative CB edge, which might be another reason for the highest photocatalytic activity as photo-generated electrons will have the highest reducing power compared to other samples.

In light of above results and discussions, it is now worthwhile to propose an explanation for the dissimilar trend of photocatalytic activity under visible light and full range irradiation for r-Sr₂FeTaO₆, r-Sr₃FeTaO₇ and r-Sr₄FeTaO₈. According to UV-vis spectra, all samples have a high absorption coefficient for ultraviolet photons and in turn a short absorption depth, therefore electrons/holes are mainly generated at the top surface of these samples, which are easier to migrate to surface reaction sites and participate in photocatalytic reactions. A higher concentration of transition metals (i.e. Fe and Ta) in the structure is favorable for a high photocatalytic activity as electrons/holes generation occurs via $\text{O}^{2-} \rightarrow \text{Ta}^{5+}$, $\text{O}^{2-} \rightarrow \text{Fe}^{3+}$ and $2\text{Fe}^{3+} \rightarrow \text{Fe}^{2+} + \text{Fe}^{4+}$ charge transfers. This explains the decrease trend in photocatalytic activity from r-Sr₂FeTaO₆ to r-Sr₄FeTaO₈ under full range irradiation. However, under visible light irradiation, the small absorption coefficient of visible light photons for all samples suggest a long absorption depth, thereby electrons/holes are likely to be generated deep inside the materials and are difficult to approach surface reaction sites due to severe charge recombination. In this regard, RP compounds with laminated structure owns considerable merits in terms of preventing inter-layer charge recombination as charge migration is restricted to every single layer of Fe(Ta)O₆ octahe-

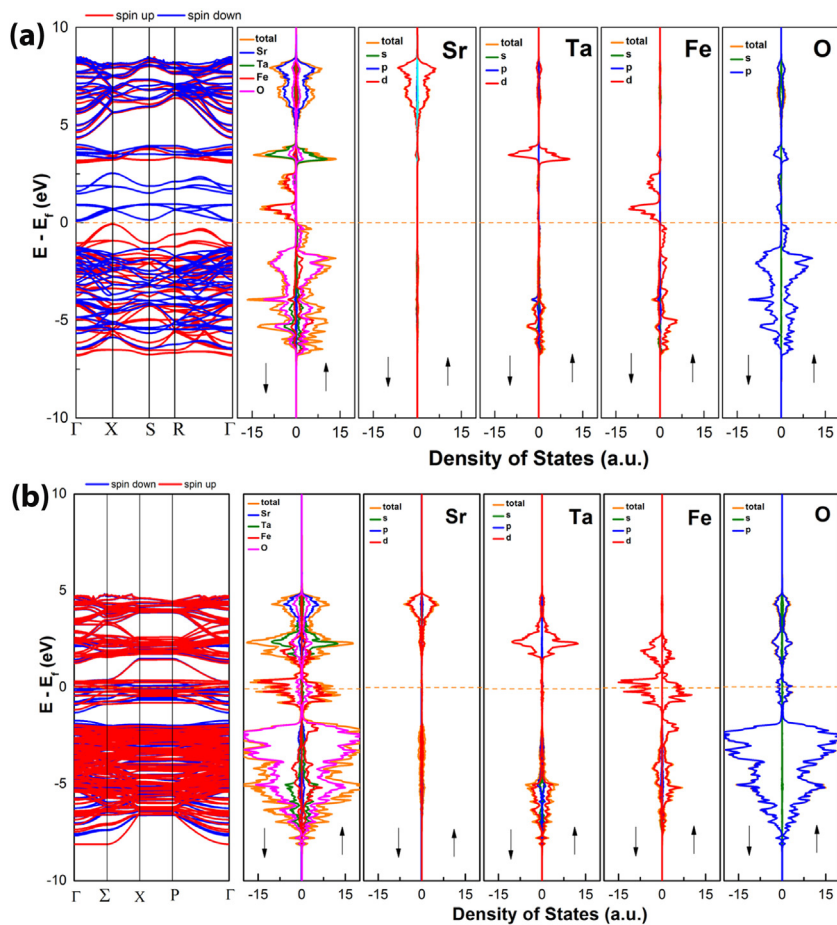


Fig. 8. Calculated band structure, total density of states (DOS) and partial density of states (PDOS) of constituent elements for $\text{Sr}_2\text{FeTaO}_6$ (a) and $\text{Sr}_4\text{FeTaO}_8$ (b).

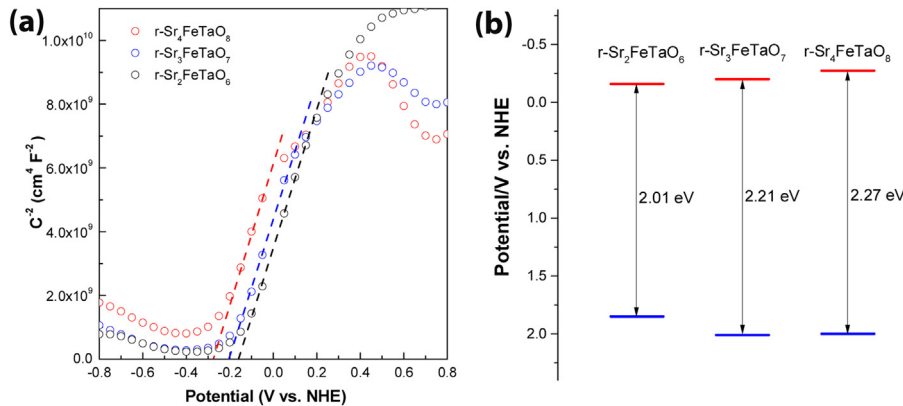


Fig. 9. (a) Mott-Schottky plot for the photoelectrodes made of sample powders after reduction, capacitance was extracted from the impedance analysis at fixed frequency of 1000 Hz with 10 mV amplitude. (b) Schematic representation of band edge positions of samples after reduction.

drons. In addition, structural lamination seems to be helpful for uplifting the CB edge where photo-generated electrons will have a high reducing power. These well explain the increasing trend of photocatalytic activity observed from $\text{r-Sr}_2\text{FeTaO}_6$ to $\text{r-Sr}_4\text{FeTaO}_8$ under visible light irradiation.

4. Conclusions

We have prepared double perovskite compound $\text{Sr}_2\text{FeTaO}_6$ and its Ruddlesden-Popper (RP) derivatives $\text{Sr}_3\text{FeTaO}_7$ and $\text{Sr}_4\text{FeTaO}_8$ via a polymeric citrate precursor method. The as-prepared samples

after high temperature calcination contain high oxidation state Fe species which gives sample powders a dark green color. A thermal treatment in ethylene glycol effectively removes those species and turns all samples into a bright yellow color. Crystal structures and microstructures are generally maintained before and after the thermal treatment and RP compounds are characterized by their peculiar layered textures. Photocatalytic hydrogen production experiments reveal the importance of the thermal treatment in boosting hydrogen production of all samples. The highest activity under full range irradiation belongs to double perovskite compound $\text{Sr}_2\text{FeTaO}_6$, which gives an average hydrogen production

rate $\sim 107 \mu\text{mol}/\text{h}$ after thermal treatment, corresponding to apparent quantum efficiency (AQE) $\sim 1.36\%$. Visible light photocatalytic hydrogen production was also realized in these samples after thermal treatment and was found to be strongly correlated to the level of structural lamination, i.e. high level of structural lamination corresponds to high activity. The best activity recorded under visible light irradiation belongs to $\text{Sr}_4\text{FeTaO}_8$ with an average hydrogen production rate $\sim 22 \mu\text{mol}/\text{h}$, corresponding to apparent quantum efficiency (AQE) $\sim 0.54\%$. Theoretical calculations reveal the anisotropic character of RP compounds in charge migration which helps to reduce charge recombination and favors high activity. The dissimilar trend in photocatalytic performance of these samples under full range and visible light irradiation can be attributed to the different generation depth of electrons/holes under ultraviolet and visible light irradiation whose charge recombination show different level of reliance toward structural lamination.

Acknowledgements

We thank Young Scientists Fund of the National Natural Science Foundation of China (Grant No. 21401142) for funding and Recruitment Program of Global Youth Experts (1000 plan). The work was supported by Shanghai Science and Technology Commission (14DZ2261100) and the Fundamental Research Funds for the Central Universities.

Appendix A. Supplementary data

Supplementary data associated with this article can be found, in the online version, at <http://dx.doi.org/10.1016/j.apcatb.2017.01.011>.

References

- [1] Annual Energy Outlook 2014, U. S. Energy Information Administration, 2014.
- [2] B. Dudley, BP Statistical Review of World Energy June 2014, 2014.
- [3] N.S. Lewis, D.G. Nocera, *P. Natl. Acad. Sci. U. S. A.* **103** (2006) 15729–15735.
- [4] X.X. Xu, C. Randorn, P. Efstatouli, J.T.S. Irvine, *Nat. Mater.* **11** (2012) 595–598.
- [5] X.X. Xu, G. Liu, C. Randorn, J.T.S. Irvine, *Int. J. Hydrogen Energy* **36** (2011) 13501–13507.
- [6] K. Maeda, K. Teramura, D.L. Lu, T. Takata, N. Saito, Y. Inoue, K. Domen, *Nature* **440** (2006) 295–295.
- [7] X.C. Wang, K. Maeda, A. Thomas, K. Takanabe, G. Xin, J.M. Carlsson, K. Domen, M. Antonietti, *Nat. Mater.* **8** (2009) 76–80.
- [8] X.X. Xu, G. Liu, A.K. Azad, *Int. J. Hydrogen Energy* **40** (2015) 3672–3678.
- [9] M.L. Lv, S. Ni, Z. Wang, T.C. Cao, X.X. Xu, *Int. J. Hydrogen Energy* **41** (2016) 1550–1558.
- [10] G.W. Cui, W. Wang, M.Y. Ma, J.F. Xie, X.F. Shi, N. Deng, J.P. Xin, B. Tang, *Nano Lett.* **15** (2015) 7199–7203.
- [11] X.Y. Xia, N. Deng, G.W. Cui, J.F. Xie, X.F. Shi, Y.Q. Zhao, Q. Wang, W. Wang, B. Tang, *Chem. Commun.* **51** (2015) 10899–10902.
- [12] O. Khaselev, J.A. Turner, *Science* **280** (1998) 425–427.
- [13] J. Liu, Y. Liu, N.Y. Liu, Y.Z. Han, X. Zhang, H. Huang, Y. Lifshitz, S.T. Lee, J. Zhong, Z.H. Kang, *Science* **347** (2015) 970–974.
- [14] S.S. Mao, X.B. Chen, L. Liu, P.Y. Yu, *Science* **331** (2011) 746–750.
- [15] Z.B. Chen, T.F. Jaramillo, T.G. Deutsch, A. Kleiman-Shwarzstein, A.J. Forman, N. Gaillard, R. Garland, K. Takanabe, C. Heske, M. Sunkara, E.W. McFarland, K. Domen, E.L. Miller, J.A. Turner, H.N. Dinh, *J. Mater. Res.* **25** (2010) 3–16.
- [16] A. Kudo, Y. Miseki, *Chem. Soc. Rev.* **38** (2009) 253–278.
- [17] Y.H. Xie, F.F. Wu, X.Q. Sun, H.M. Chen, M.L. Lv, S. Ni, G. Liu, X.X. Xu, *Sci. Rep.* **5** (2016) 19060.
- [18] Y.H. Xie, Y.W. Wang, Z.F. Chen, X.X. Xu, *ChemSusChem* **9** (2016) 1403–1412.
- [19] F.F. Wu, M.L. Lv, X.Q. Sun, Y.H. Xie, H.M. Chen, S. Ni, G. Liu, X.X. Xu, *ChemCatChem* **8** (2016) 615–623.
- [20] L.W. Lu, M.L. Lv, G. Liu, X.X. Xu, *Appl. Surf. Sci.* **391** (2017) 535–541.
- [21] X.Q. Sun, Y.H. Xie, F.F. Wu, H.M. Chen, M.L. Lv, S. Ni, G. Liu, X.X. Xu, *Inorg. Chem.* **54** (2015) 7445–7453.
- [22] X.Q. Sun, S.W. Wang, C. Shen, X.X. Xu, *ChemCatChem* **8** (2016) 2289–2295.
- [23] X.X. Xu, A.K. Azad, J.T.S. Irvine, *Catal. Today* **199** (2013) 22–26.
- [24] X.X. Xu, Y.H. Xie, S. Ni, A.K. Azad, T.C. Cao, *J. Solid State Chem.* **230** (2015) 95–101.
- [25] X.X. Xu, M.L. Lv, X.Q. Sun, G. Liu, *J. Mater. Sci.* **51** (2016) 6464–6473.
- [26] Y. Ham, T. Hisatomi, Y. Goto, Y. Moriya, Y. Sakata, A. Yamakata, J. Kubota, K. Domen, *J. Mater. Chem. A* **4** (2016) 3027–3033.
- [27] F.T. Wagner, G.A. Somorjai, *Nature* **285** (1980) 559–560.
- [28] M.L. Lv, Y.W. Wang, L.W. Lu, R.N. Wang, S. Ni, G. Liu, X.X. Xu, *Phys. Chem. Chem. Phys.* **18** (2016) 21491–21499.
- [29] S. Ida, Y. Okamoto, M. Matsuka, H. Hagiwara, T. Ishihara, *J. Am. Chem. Soc.* **134** (2012) 15773–15782.
- [30] K. Maeda, K. Domen, *Angew. Chem. Int. Ed.* **51** (2012) 9865–9869.
- [31] A. Kudo, H. Kato, S. Nakagawa, *J. Phys. Chem. B* **104** (2000) 571–575.
- [32] M. Hojaberdi, M.F. Bekheet, E. Zahedi, H. Wagata, J.J.M. Vequiza, A. Yamakata, K. Yubuta, A. Gurlo, K. Domen, K. Teshima, T. Dalton, *(2016) 12559–12568*.
- [33] C.Z. Wang, T. Hisatomi, T. Minegishi, Q. Wang, M. Zhong, M. Katayama, J. Kubota, K. Domen, *J. Phys. Chem. C* **120** (2016) 15758–15764.
- [34] H. Kato, K. Asakura, A. Kudo, *J. Am. Chem. Soc.* **125** (2003) 3082–3089.
- [35] R.H. Mitchell, *Perovskites: Modern and Ancient*, Almaz Press Inc., Ontario, Canada, 2002.
- [36] J. Yin, Z.G. Zou, J.H. Ye, *J. Phys. Chem. B* **108** (2004) 8888–8893.
- [37] C.S. Pan, T. Takata, M. Nakabayashi, T. Matsumoto, N. Shibata, Y. Ikuhara, K. Domen, *Angew. Chem. Int. Ed.* **54** (2015) 2955–2959.
- [38] B. Xu, W.F. Zhang, X.Y. Liu, J.H. Ye, W.H. Zhang, L. Shi, X.G. Wan, J. Yin, Z.G. Liu, *Phys. Rev. B* **76** (2007).
- [39] P.V.d. Heide, John Wiley & Sons, Inc, Hoboken, New Jersey (2012).
- [40] G. Kresse, J. Furthmuller, *Phys. Rev. B* **54** (1996) 11169–11186.
- [41] J.P. Perdew, K. Burke, M. Ernzerhof, *Phys. Rev. Lett.* **77** (1996) 3865–3868.
- [42] G. Kresse, D. Joubert, *Phys. Rev. B* **59** (1999) 1758–1775.
- [43] H.J. Monkhorst, J.D. Pack, *Phys. Rev. B* **13** (1976) 5188–5192.
- [44] A.R. West, *Solid State Chemistry and Its Applications*, Wiley India Pvt. Limited, 2007.
- [45] M. Ghaffari, H. Huang, O.K. Tan, M. Shannon, *CrystEngComm* **14** (2012) 7487–7492.
- [46] M.L. Lv, Y.H. Xie, Y.W. Wang, X.Q. Sun, F.F. Wu, H.M. Chen, S.W. Wang, C. Shen, Z.F. Chen, S. Ni, G. Liu, X.X. Xu, *Phys. Chem. Chem. Phys.* **17** (2015) 26320–26329.
- [47] L.W. Lu, M.L. Lv, D. Wang, G. Liu, X.X. Xu, *Appl. Catal. B-Environ.* **200** (2017) 412–419.
- [48] T. Ishii, H. Kato, A. Kudo, *J. Photochem. Photobiol. A* **163** (2004) 181–186.
- [49] P.A. Cox, *The Electronic Structure and Chemistry of Solids*, Oxford University Press, 1987.
- [50] C. Kittel, *Introduction to Solid State Physics*, 7th ed., Wiley, New York, 1996.
- [51] H. Mizoguchi, P.M. Woodward, *Chem. Mater.* **16** (2004) 5233–5248.
- [52] M.L. Lv, G. Liu, X.X. Xu, *ACS Appl. Mater. Interfaces* **8** (2016) 28700–28708, <http://dx.doi.org/10.1021/acsami.1026b10951>.